

Three-dimensional supersonic flow around double compression ramp with finite span

H. S. Lee¹ · J. H. Lee¹ · G. Park² · S. H. Park¹ · Y. H. Byun¹

Received: 10 November 2014 / Revised: 20 January 2016 / Accepted: 13 February 2016 / Published online: 15 March 2016
© Springer-Verlag Berlin Heidelberg 2016

Abstract Three-dimensional flows of Mach number 3 around a double-compression ramp with finite span have been investigated numerically. Shadowgraph visualisation images obtained in a supersonic wind tunnel are used for comparison. A three-dimensional Reynolds-averaged Navier–Stokes solver was used to obtain steady numerical solutions. Two-dimensional numerical results are also compared. Four different cases were studied: two different second ramp angles of 30° and 45° in configurations with and without sidewalls, respectively. Results showed that there is a leakage of mass and momentum fluxes heading outwards in the spanwise direction for three-dimensional cases without sidewalls. The leakage changed the flow characteristics of the shock-induced boundary layer and resulted in the discrepancy between the experimental data and two-dimensional numerical results. It is found that suppressing the flow leakage by attaching the sidewalls enhances the two-dimensionality of the experimental data for the double-compression ramp flow.

Keywords Computational fluid dynamics · Supersonic flow · Shock wave/boundary layer interaction · Double-compression ramp

1 Introduction

Shock wave/boundary layer interactions have been investigated by many researchers because the interaction may cause boundary layer instabilities and high thermal loads over a supersonic vehicle. Such a physical phenomenon is often observed when the flow travels around a double-compression ramp that is usually encountered in a scramjet inlet or a wing-body intersection. When the shock wave induces a separation bubble that is formed by an adverse pressure gradient, several different types of shock wave/boundary layer interactions occur along with the shock wave ahead of the separation bubble.

Numerical simulation of supersonic flow over a double-compression ramp with finite span is a challenging topic not only because of the three-dimensional complexity [1–4], but also due to turbulent transition inside the separation bubble [5,6], and/or numerical difficulties [7]. In his study of shock–shock interactions between an oblique shock and a bow shock over a cylinder, Edney [8] identified six different types of shock–shock interactions. Types IV, V, and VI in particular represent typical shock–shock interactions that are often produced in double-compression ramp flows. A single shock deflects the flow along the second ramp when the second ramp angle has a smaller angle than the maximum deflection angle of the freestream flow. The maximum deflection angle is defined as the angle when the oblique shock is no longer attached to the corner. This is categorised as the type VI interaction. The type V interaction occurs when the second ramp angle is large, and as a result, the freestream flow is not deflected by a single shock. The type IV shock interaction occurs when the second ramp angle is increased further and when the oblique shocks at the first and the second ramp junctions are unable to provide appropriate downstream flow conditions so that a normal shock is formed upstream of

Communicated by F. Lu and A. Higgins.

✉ S. H. Park
pish@konkuk.ac.kr

¹ Department of Aerospace Information Engineering, Konkuk University, Hwayang-dong, Gwangjin-gu, Seoul, South Korea

² Division of Aerospace Engineering, Korea Advanced Institute of Science and Technology, Guseong-dong, Yuseong-gu, Daejeon, South Korea

a compression corner. The terminologies have been widely adopted and analysed in detail in previous studies [9, 10].

Häberle and Gülhan [3] showed the occurrence of heat load in a scramjet inlet flow experimentally as well as numerically for cases with and without sidewalls. They found that numerical results using a transition model showed a better agreement with the experiment than the results generated using a turbulence model. Numerical simulations for the effect of sidewall compression have been conducted [11–13]. Recently, Schrijer [10] experimentally and numerically studied physical phenomena over a double-compression ramp at a Mach number of 7. He showed that numerical results are different from the experiment due to a three-dimensional (3-D) effect when the oblique shock wave is detached from the corner. Grasso et al. [14] demonstrated that a poor distribution of an upstream influence on the center of the boundary layer can result in a different outcome along the spanwise direction when two-dimensional (2-D) results are compared with those of the 3-D case. They showed that the separation region can be reduced by a finite span, for a single compression ramp, with a decrease in peak pressure and heat transfer. Due to the 3-D effect over the compression ramp with a finite span, it is quite difficult to guarantee a two-dimensionality of the experimental data. A sufficient length in the spanwise direction can be considered to suppress the 3-D effect, but it is limited because of the available size of the test section.

At present, most of the previous studies investigated the 3-D effect for single compression ramps at high Mach numbers. It is necessary to understand the 3-D effect at relatively low Mach numbers using a practical model such as a double compression ramp. Turbulent flows of Mach number 3 around the double-compression ramp for different ramp angles, therefore, were numerically investigated herein. Shadowgraph images obtained in a supersonic wind tunnel are compared with the present numerical results. At the Mach number considered, different types of shock wave/boundary layer interaction can be generated as a function of the ramp angle. And the 3-D effect due to the finite span is remarkable at relatively low Mach numbers. Reynolds-averaged Navier–Stokes (RANS) simulations with a k - ω SST turbulence model were performed for four different cases: two different second ramp angles of 30° and 45° with respect to the freestream direction, each with and without the sidewalls, respectively.

2 Numerical details

2.1 Numerical method

The three-dimensional flows were computed using the compressible RANS equations and a k - ω turbulence model. The

equations can be written in the conservative form as follows:

$$\frac{\partial Q}{\partial t} + \frac{\partial(f_j - f_{vj})}{\partial x_j} = S_{k\omega} \quad j = 1, 2, 3. \quad (1)$$

$$Q = [\rho, \rho u_i, \rho e_t, \rho k, \rho \omega]^T \quad (2)$$

where Q is the conservative variable vector, f_j and f_{vj} represent inviscid and viscous flux vectors in the x_j direction, respectively. ρ is the density, u_i is the velocity component in each direction, e_t is the total energy, k is the turbulence kinetic energy, ω is the specific dissipation rate, and $S_{k\omega}$ is the source term of the turbulence model. The governing equations were discretized using the cell-centered finite volume method. The advection upstream splitting method using pressure weighting (AUSMPW+) [15] and the second-order accurate monotonic upstream-centered scheme for conservation laws (MUSCL) with the minmod limiter were used to compute inviscid flux functions at each cell interface. Viscous fluxes were discretized by the second-order central difference scheme. A second-order dual-time stepping method coupled with a diagonalized alternating directional implicit (ADI) scheme [16] was applied. Menter's k - ω shear-stress-transport (SST) model [17] was adopted for the turbulence closure.

Figure 1 displays the 3-D grid system with a uniform spacing along the spanwise direction (z -direction). The grid was made with a distance of 1.0×10^{-6} m from the first cell center to the ramp wall, which corresponds to a nondimensional wall distance of $y^+ < 1$. The number of cells has a dimension of 400 (streamwise) \times 300 (normal to the ramp wall) \times 100 (spanwise). Freestream values were set at the inflow boundaries. All flow variables at the outflow boundaries were extrapolated from the interior cells. To take into account the sidewalls, 35 mm high walls were inserted at both sides of the span edge for the case with the sidewalls, as shown in Fig. 1. The isothermal no-slip boundary condition was applied at the ramp surfaces and the wall temperature was set to 290 K. The slip-wall boundary condition was applied to the sidewalls, since the blockage effect due to the sidewalls was only considered in the present work. Additional computations are required with the no-slip wall condition to further quantify the viscous effects due to sidewalls.

A grid convergence study was carried out for the 2-D case of 15°–45° (first/second stage ramp angles) configuration. Figures 2 and 3 compare the wall pressure and the skin friction coefficient for three different grid densities: coarse (301 \times 201), medium (401 \times 301), and fine (501 \times 401) grids. Unsteady computations were performed until converged to their steady-state solutions. From the figures, it can be seen that there is a negligible difference between results from fine and medium grids. Results from the coarse grid show a noticeable difference in the prediction of the shock wave/boundary layer interaction from the other cases due to the inadequate number of grid points in the x - and

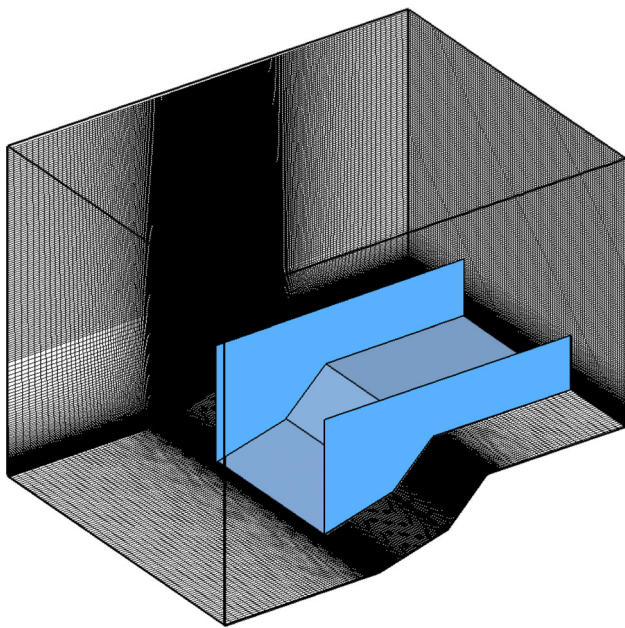


Fig. 1 Schematic of 3-D double-compression ramp with sidewalls (15° – 45°)

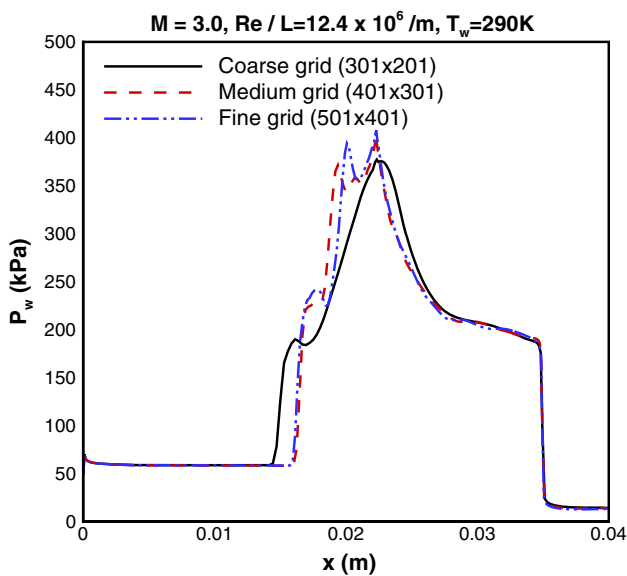


Fig. 2 Grid convergence of wall static pressure

y-directions. It was concluded that the medium grid is appropriate for the present computations, and the 3-D grids were generated by extending the medium grid with 101 grid points in the spanwise direction.

2.2 Validation

The efficacy of the present numerical schemes used was validated for a 10° impinging shock problem. Flow conditions used in Ref. [18] were $M_\infty = 5.0$ and $Re/L = 3.76 \times 10^6/m$.

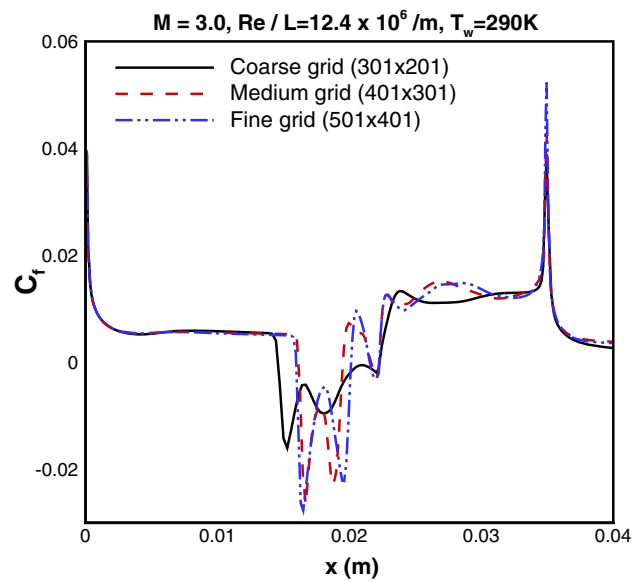


Fig. 3 Grid convergence of skin friction coefficient

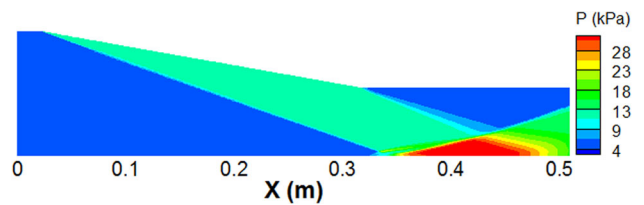


Fig. 4 Pressure contour of 10° impinging shock problem

The present results were compared with the computational results of Brown [19] as well as the experimental data. The nondimensional distance of the first cell from the wall was 1.0×10^{-6} , which corresponds to the nondimensionalized wall distance of about $y^+ = 1$. The total number of cells was 90,000. The isothermal wall boundary condition was applied and the wall temperature was set to 278 K.

As shown in Fig. 4, a 10° shock generator at the leading edge of the upper wall produces an oblique shock wave that interacts with a turbulent boundary layer over the lower surface. This leads to the formation of a separation bubble. An induced shock wave by the separation bubble interacts again with the boundary layer and the oblique shock. The top of Fig. 5 shows the pressure distribution along the lower surface. The oblique shock that is produced at the upper surface impinges at $x = 0.35$. The pressure coefficients are steeply increased near the separation point. A moderate increase in the pressure coefficient after the impingement point shows a similar variation to the experimental data. The skin friction coefficient distribution, shown at the bottom of Fig. 5, shows that both the computational results predict well the separation region that is denoted by the negative skin friction coefficient. Compared to the experiment, the numerical results show lower magnitudes in the skin friction coefficient

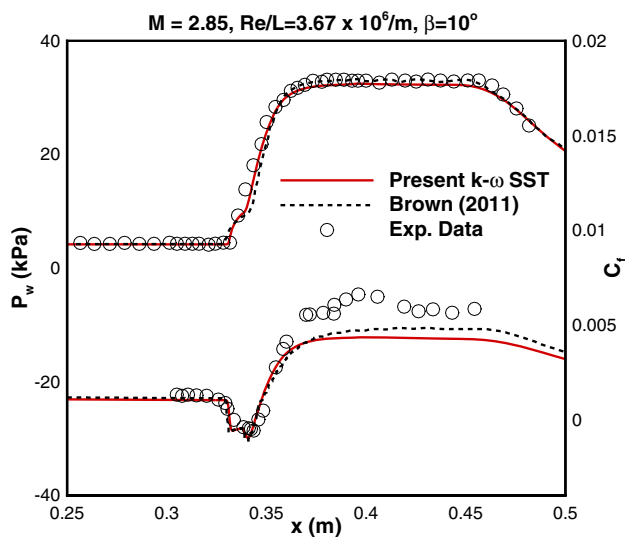


Fig. 5 Comparison of wall static pressure (*top*) and skin friction coefficient (*bottom*) for the 10° impinging shock problem

after the reattachment region. This is caused from the inaccurate prediction of the turbulent kinetic energy for the $k-\omega$ SST turbulence model.

3 Wind tunnel experiment

The experiment was conducted using a model aerodynamic facility (MAF) in Konkuk University. The MAF is a supersonic wind tunnel facility that can produce flow Mach numbers from 2 to 7. In this work, the flow conditions were $M_\infty = 3.0$, $P_\infty = 20,417$ Pa, $T_\infty = 103$ K, and $Re/L = 12.4 \times 10^6/m$. The size of the optical window has a dimension of 285 mm (length) \times 135 mm (height) and the spanwise width of the test section is 226 mm. The 15° – 30° model has a length of 40 and 23.7 mm for the first and the second ramps, respectively. The 15° – 45° model has a length of 23 and 18 mm for the first and the second ramps, respectively. Both models have the same width of 81 mm. Flow visualisation images were obtained using a standard shadowgraph technique. A PCO 1600 high-speed camera and an 80 W capacity LED lamp light source were used. Data were obtained at a frequency of 32 Hz. The MAF operation time was about 1.5 s.

Figure 6 displays typical shadowgraph images for the 15° – 30° and the 15° – 45° cases. Figure 6a shows that the 15° – 30° case has a small separation region because the second ramp angle is relatively smaller than the maximum deflection angle. This leads to the weak compression at the corner and so the interaction between the shock wave and the boundary layer seems to be marginal. Weak oblique shock waves from the nozzle exit interacted with the flow around the model at different locations since the 15° – 45° model was located

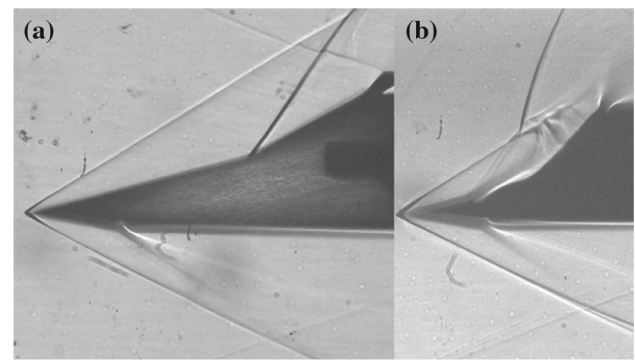


Fig. 6 Experimental shadowgraph images; **a** 15° – 30° and **b** 15° – 45° double-compression ramp

further upstream than the 15° – 30° model. It should be noted that the oblique shock waves that emanated from the nozzle exit in the wind tunnel did not affect the flow characteristics. As shown in Fig. 6b, the second ramp angle of the 15° – 45° case is high enough to produce a large separation due to the adverse pressure gradient at the corner. As a result, a separation shock is produced ahead of the corner. A reattachment shock is also generated where the separated flow reattaches to the second ramp wall. A strong curved shock wave is formed after both the separation shock and the reattachment shock intersect with the shock wave that is emanated from the leading edge.

4 Results and discussion

4.1 15° – 30° case

Figure 7 compares experimental and numerical shadowgraph images for the 15° – 30° double-compression ramp case. Numerical shadowgraph results were obtained for four cases: (b) 2-D case, 3-D cases (c) without and (d) with the sidewalls, and (e) 3-D case with double-span length that will be discussed in Sect. 4.3. Definition of the numerical shadowgraph used is given below:

$$(\text{Numerical shadowgraph}) = \sqrt{\left(\frac{\partial^2 \rho}{\partial x^2}\right)^2 + \left(\frac{\partial^2 \rho}{\partial y^2}\right)^2} \quad (3)$$

Here, the second derivatives of the density are evaluated at the center plane of the domain. It should be noted that the present numerical shadowgraphs would not be the same as the experiments because the experimental shadowgraphs include an integrated effect of the density derivatives along the optical path length.

As shown in Fig. 7, all numerical shadowgraph images agree well with the experimental one. Wave angles of the oblique shock waves from both the leading edge and the

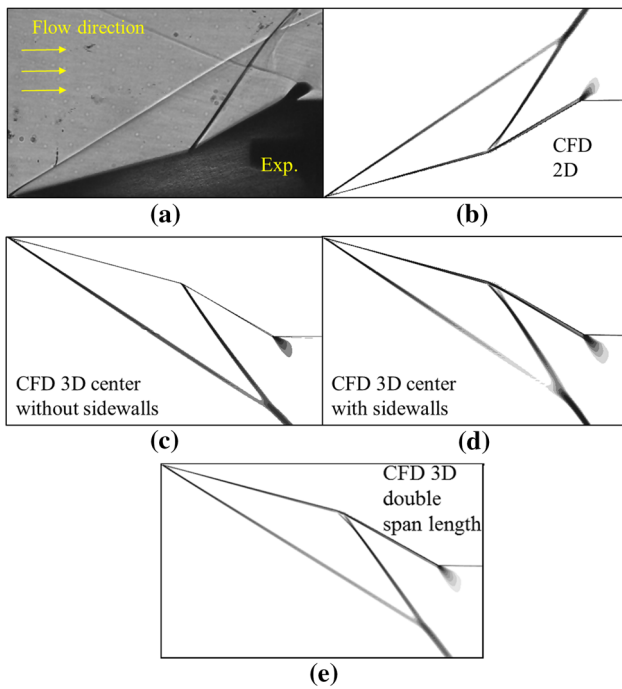


Fig. 7 Experimental and numerical shadowgraphs for 15°–30° double-compression ramp (double-span length part will be discussed in Sect. 4.3)

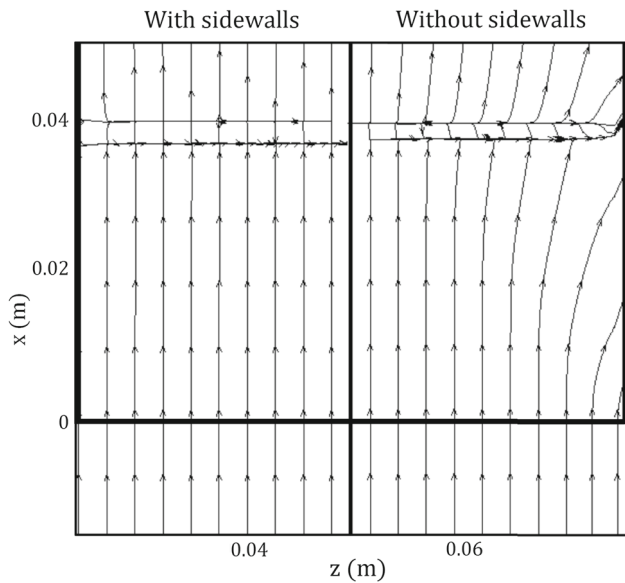


Fig. 8 Surface streamlines with sidewalls (*left*) and without sidewalls (*right*) (15°–30°)

corner of the second ramp are well matched with the experimental data in Fig. 7a. It is seen that, regardless of the sidewalls, the flow two-dimensionality in the experiment can be sustained as long as the shock wave/boundary layer interaction is not so strong. Figure 8 shows surface streamlines for the cases with and without the sidewalls. In the case of the model without the sidewalls, the streamlines near the edge

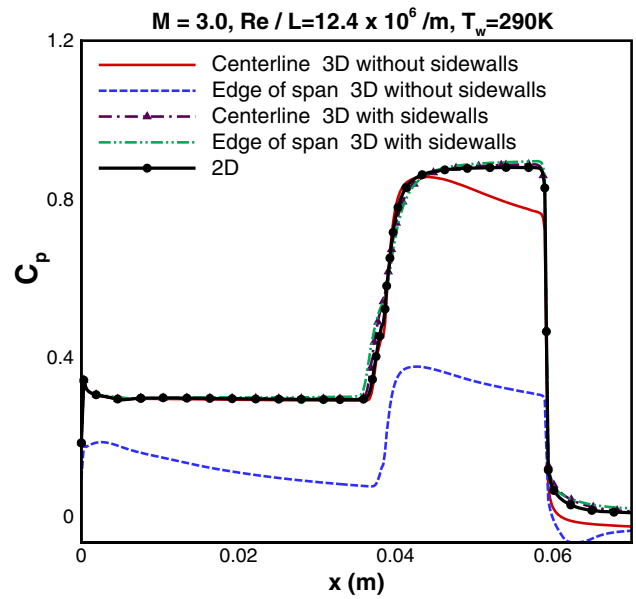


Fig. 9 Comparison of wall pressure coefficient for each of the three models (15°–30°)

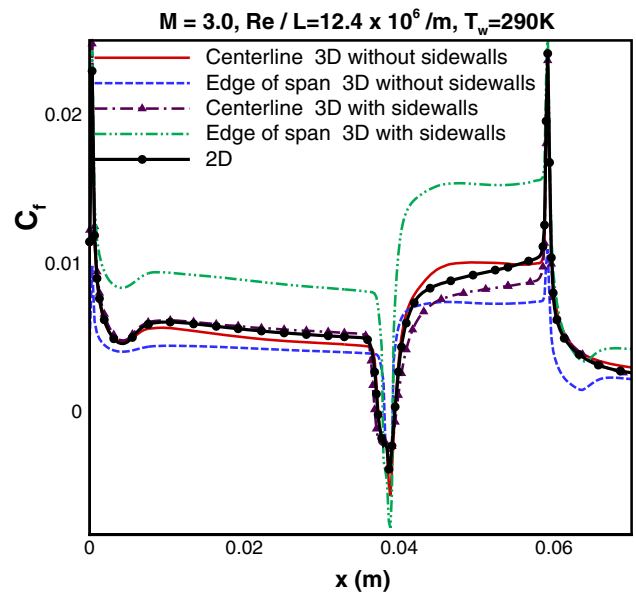


Fig. 10 Comparison of skin friction coefficient for each of the three models (15°–30°)

of the span head outwards with a small curvature. The separation shock also forms in a curved shape due to a flow leakage at the edge of the span. In the case with the sidewalls, streamlines remain straight downstream without the flow leakage and the separation region takes a uniform shape along the spanwise direction. There is a marginal difference in the extent of the separation bubble between the two models.

Figures 9 and 10 compare the wall pressure and the skin friction coefficients. Distributions of the wall coefficients at

the centerline and the edge of the span for cases with and without the sidewalls are compared with the 2-D computational data. A separation bubble at the ramp corner, which is denoted by negative values in Fig. 10, is produced due to the adverse pressure gradient. For the case without the sidewalls, overall magnitudes of the pressure and the skin friction at the edge of the span are much different from the others. However, the pressure distribution along the centerline follows well the 2-D distribution just before the reattachment of the separation bubble. It should be noted that for the case with the sidewalls, the pressure distributions at every spanwise location between the sidewalls are nearly the same as the 2-D distribution. All numerical results have a similar extent of the separation at the centerline regardless of the presence of the sidewalls. It is found, therefore, that a localized three-dimensional effect exists near the edge of the span, but such a small change is not able to alter the essential characteristics of the 15° – 30° ramp flow.

4.2 15° – 45° case

Compared to the 15° – 30° case, the 15° – 45° case produces a large separation bubble and consequently stronger shock wave/boundary layer interaction in the flow field. Figure 11 shows the experimental and numerical shadowgraphs of the 3-D cases with and without the sidewalls. The differences in the oblique shock wave angles at the leading edge are mar-

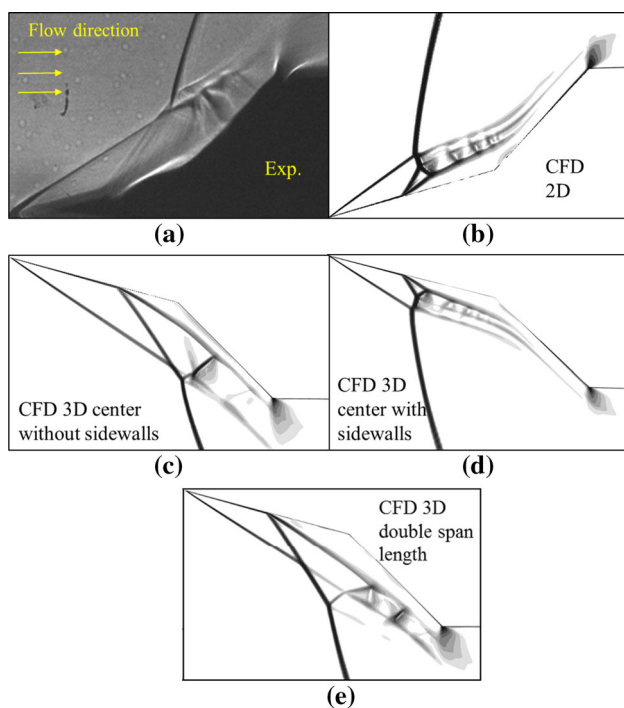


Fig. 11 Experimental and numerical shadowgraphs for 15° – 45° double compression ramp (double-span length part will be discussed in Sect. 4.3)

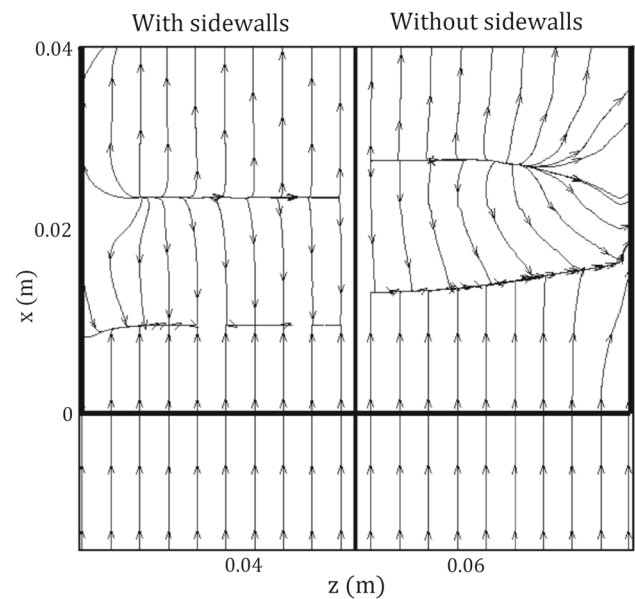


Fig. 12 Surface streamlines with sidewalls (*left*) without sidewalls (*right*) (15° – 45°)

ginal for all four cases, whereas for the case with the sidewalls the position of the separation shock and the flow characteristics behind the post-shock wave are significantly different from those for the 3D cases without the sidewalls. The 3-D case without the sidewalls in Fig. 11c shows essentially a similar type of interactions to the experiment in view of the flow structure of shock waves and shear layers. It should be noted that the 3-D case with the sidewalls shows almost the same flow structure as that of the 2-D case. This indicates that the experimental data contain the 3-D effect due to the finite span of the model. Furthermore, the implementation of the sidewalls greatly enhances the two-dimensionality of the flow.

It is found that there is a leakage of mass and momentum fluxes heading outward in the spanwise direction, mainly in the vicinity of the separation bubble for the 3-D case without the sidewalls. The 3-D leakage effect is examined further in Fig. 12 that compares surface streamlines for the cases with and without the sidewalls. The losses of mass and momentum fluxes are caused by the 3-D distortion of the flow field which represents a non-uniform pressure gradient along the spanwise direction. Similar to the 15° – 30° case in Fig. 8, the 15° – 45° case without the sidewalls in Fig. 12 shows that the streamlines go through the edge side and the separation region becomes narrow toward the edge. However, in the case with the sidewalls, the flow in the separation region is restricted by the blockage of the sidewalls. Consequently, the separation bubble forms a nearly uniform shape. This is why the two-dimensionality of the experimental data seems enhanced by applying the sidewalls.

Figures 13 and 14 compare distributions of the pressure and the skin friction coefficients. The variations of the

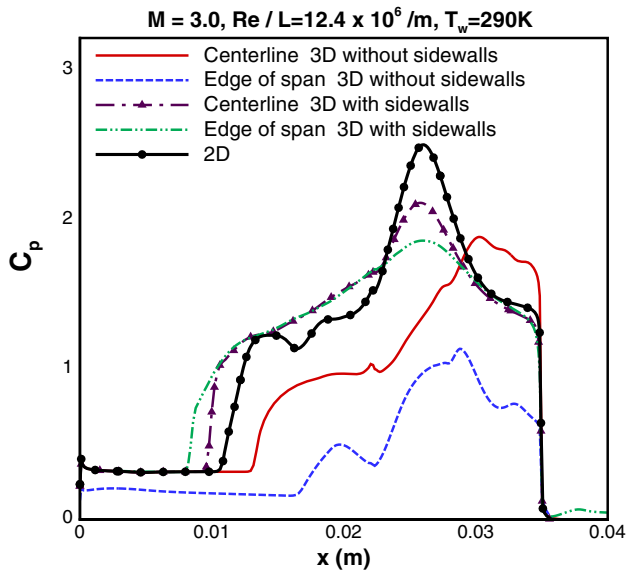


Fig. 13 Comparison of wall pressure coefficient for each of the three models (15°–45°)

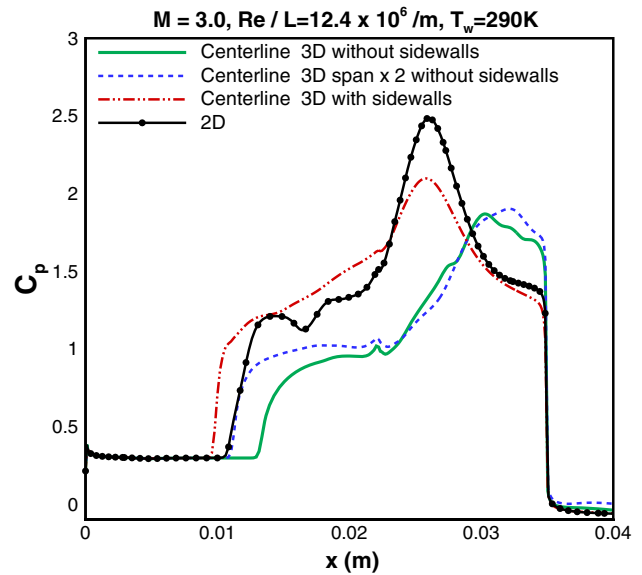


Fig. 15 Effect of the span length of the 15°–45° model: wall pressure coefficient

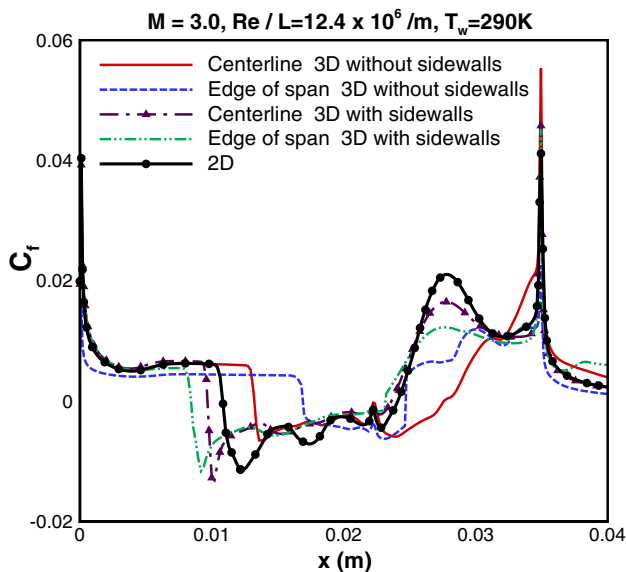


Fig. 14 Comparison of skin friction coefficient for each of the three models (15°–45°)

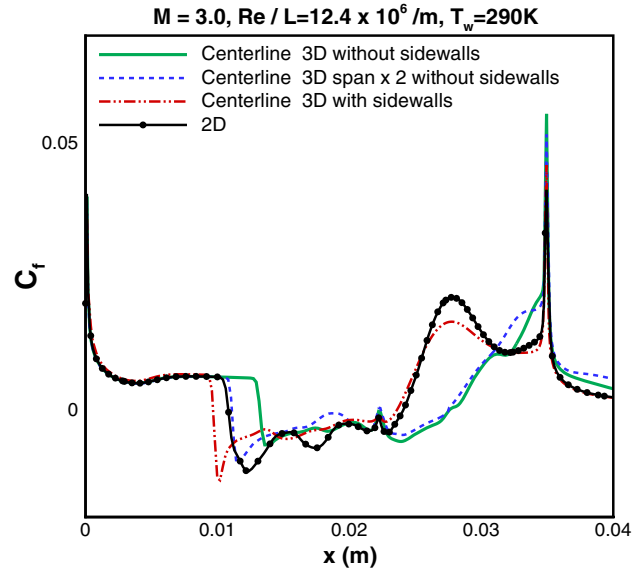


Fig. 16 Effect of the span length of the 15°–45° model: skin friction coefficient

wall coefficients for the 3-D model with the sidewalls are essentially similar to those of the 2-D case, although the distributions are not identical. But, the pressure coefficients for the 3-D model without the sidewalls are quite less than those with the sidewalls. This implies that a spanwise pressure gradient is generated for the case without the sidewalls. The extent of the separation bubble for the case without the sidewalls is smaller than that with the sidewalls. The flux leakage begins from the leading edge under the spanwise pressure gradient and consequently the boundary layer is likely to attach farther to the wall. The present investigation demon-

strates that the 3-D effect in the double-compression ramp with finite span is strongly related to the pressure distribution near the edge of the model.

4.3 Three-dimensional leakage effect

Further investigations were carried out to explain the 3-D leakage effect by doubling the spanwise length of the model without the sidewalls. Surface distributions of the pressure and the skin friction coefficients are compared in Figs. 15 and 16. The location of the separation has moved upstream

Table 1 Ratios of mass and momentum effluxes through the side plane at the edge station

	Without sidewalls		With sidewalls		Double-span length	
	Mass flux (%)	Momentum flux (%)	Mass flux (%)	Momentum flux (%)	Mass flux (%)	Momentum flux (%)
15°–30°	–21.3	–2.9	–0.4	–0.2	–11.3	–1.6
15°–45°	–27.8	–4.4	–1.5	–0.2	–18.3	–3.1

toward the separation location for the case with the sidewalls. This means that the three-dimensionality due to the finite span is somewhat relaxed by doubling the span length. However, the distributions of the pressure and skin friction coefficients are similar to those for the case without the sidewalls, despite the fact that the span length is doubled in the spanwise direction.

The relative amount of the flow leakage through the edge side of each 3-D model was calculated and compared in Table 1. The ratios of the mass efflux \dot{m}_z and the momentum efflux \dot{M}_z to the freestream values are defined as follows:

$$\dot{m}_z/\dot{m}_{\text{inlet}} (\%) = 100 \int \rho \mathbf{V} \cdot d\mathbf{A}_z / (\rho_{\infty} U_{\infty} A_{\text{inlet}}) \quad (4)$$

$$\dot{M}_z/\dot{M}_{\text{inlet}} (\%) = 100 \int -w(\rho \mathbf{V} \cdot d\mathbf{A}_z) / (\rho_{\infty} U_{\infty}^2 A_{\text{inlet}}), \quad (5)$$

where \dot{m}_z and \dot{M}_z are mass and momentum fluxes, w and \mathbf{A}_z represent the spanwise component of the velocity and the area of the vertical plane at the edge station, respectively. A_{inlet} denotes the projected cross section area of each model. It is noted that higher efflux means larger flow leakage through the edge side of the model. As shown in Table 1, the mass and the momentum effluxes are reduced by doubling the span length. On the other hand, the effluxes are so small that the effect is negligible when the sidewalls are implemented. The flow leakage through the edge side of the 15°–45° model is larger than that of the 15°–30° model, regardless of the span length. This implies that the three-dimensionality of the 15°–45° case is higher than that of the 15°–30° case. The present comparison is consistent with common sense that the enlargement of the span length is helpful to enhance the two-dimensionality, but the effect of the double-span length is not as powerful as the implementation of the sidewalls.

5 Conclusions

Three-dimensional effects in the double-compression ramp flows with finite span were investigated. Shadowgraph images for the 15°–30° and the 15°–45° cases were compared with computational results. The result with the sidewalls has nearly the same flow structure as that for the 2-D case, whereas the results without the sidewalls show a reasonable agreement with the experimental data. The three-

dimensionality of the experimental data can be explained by the flow leakage as a result of the spanwise pressure gradient due to the finite span length. The flow leakage changes flow characteristics of both the shock and the boundary layer and ultimately leads to the three-dimensional flow structure of the experimental data. The comparison shows that suppressing the flow leakage by attaching the sidewalls can enhance the two-dimensionality of the experimental data.

Acknowledgements This work was supported by the space core technology development program through the National Research Foundation of Korea funded by the Ministry of Science, ICT and Future Planning (No: 20110020837).

References

- Rudy, D.H., Thomas, J.L., Kumar, A., Gnoffo, P.A., Chakravarthy, S.R.: Computation of laminar hypersonic compression-corner flows. *AIAA J.* **29**(7), 1108–1113 (1991)
- Marini, M.: Analysis of hypersonic compression ramp laminar flows under sharp leading edge conditions. *Aerosp. Sci. Technol.* **5**(4), 257–271 (2001)
- Häberle, J., Gülhan, A.: Investigation of two-dimensional scramjet inlet flowfield at Mach 7. *J. Propuls. Power.* **24**(3), 446–459 (2008)
- Graur, I.A., Ivanov, M.S., Markelov, G.N., Burtschell, Y., Valerio, E., Zeitoun, D.: Comparison of kinetic and continuum approaches for simulation of shock wave/boundary layer interaction. *Shock Waves J.* **12**(4), 343–350 (2003)
- Navarro-Martinez, S., Tutty, O.R.: Numerical simulation of Görtler vortices in hypersonic compression ramps. *Comput. Fluids* **34**(2), 225–247 (2005)
- Navarro-Martinez, S.: Numerical simulation of laminar flow over hypersonic compression ramps. PhD. thesis, University of Southampton, UK (2002)
- Simeonides, G., Haase, W.: Experimental and computational investigations of hypersonic flow about compression ramps. *J. Fluid Mech.* **283**, 17–42 (1995)
- Edney, B.: Anomalous heat transfer and pressure distributions on blunt bodies at hypersonic speeds in the presence of an impinging shock. FFA, Technical Report no. 115 (1968)
- Olejniczak, J., Wright, M.J., Candler, G.V.: Numerical study of inviscid shock interactions on double-wedge geometries. *J. Fluid Mech.* **352**, 1–25 (1997)
- Schrijer, F.F.J.: Experimental investigation of re-entry aerodynamic phenomena - Development of non-intrusive flow diagnostics in a Ludwig tube. PhD. thesis. Delft University of Technology, The Netherlands (2010)
- Hohn, O., Gülhan, A.: Experimental investigation on the influence of sidewall compression on the flowfield of a scramjet inlet at Mach 7. In: 17th AIAA International Space Planes and Hyper-

- sonic Systems and Technologies Conference, AIAA 2011-2350. San Francisco (2011)
12. Nguyen, T., Behr, M., Reinartz, B., Hohn, O., Gülhan, A.: Effects of sidewall compression and relaminarization in a scramjet inlet. *J. Propuls. Power.* **29**(3), 628–638 (2013)
 13. Holland, S.D.: Computational parametric study of sidewall-compression scramjet inlet performance at Mach 10. NASA TM-4411 (1993)
 14. Grasso, F., Marini, M.: TVD multigrid solutions of three-dimensional viscous hypersonic flows. In: 33rd Aerospace Sciences Meeting and Exhibit, AIAA 1995-0470. Reno, NV (1995)
 15. Kim, K.H., Kim, C., Rho, O.H.: Methods for accurate computations of hypersonic flows: I. AUSMPW+ scheme. *J. Comput. Phys.* **174**(1), 38–80 (2001)
 16. Park, S.H., Kwon, J.H.: Implementation of k - ω turbulence models in an implicit multigrid method. *AIAA J.* **42**(7), 1348–1357 (2004)
 17. Menter, F.R.: Two-equation eddy-viscosity turbulence models for engineering applications. *AIAA J.* **32**(8), 1598–1605 (1994)
 18. Schülein, E.: Skin friction and heat flux measurements in shock/boundary layer interaction flows. *AIAA J.* **44**(8), 1732–1741 (2006)
 19. Brown, J.L.: Shock wave impingement on boundary layers at hypersonic speeds: computational analysis and uncertainty. In: 42nd AIAA Thermophysics Conference, AIAA 2011-3143. Honolulu, HI (2011)